Multiscale porous elastomer substrates for multifunctional on-skin electronics with passive-cooling capabilities

Yadong Xu[a,1], Bohan Sun[b,1], Yun Ling[b,1], Qihui Fei[a], Zanyu Chen[a], Xiaopeng Li[b], Peijun Guo[c], Nari Jeon[c], Shivam Goswami[b], Yixuan Liao[a], Shinghua Ding[a], Qingsong Yu[b], Jian Lin[b], Guoliang Huang[b,2], and Zheng Yan[a,b,2]

[a]Department of Biomedical, Biological, and Chemical Engineering, University of Missouri, Columbia, MO 65211; [b]Department of Mechanical and Aerospace Engineering, University of Missouri, Columbia, MO 65211; and [c]Materials Science Division and Center for Nanoscale Materials, Argonne National Laboratory, Lemont, IL 60439

Edited by John A. Rogers, Northwestern University, Evanston, IL, and approved November 18, 2019 (received for review October 12, 2019)

In addition to mechanical compliance, achieving the full potential of on-skin electronics needs the introduction of other features. For example, substantial progress has been achieved in creating biodegradable, self-healing, or breathable, on-skin electronics. However, the research of making on-skin electronics with passive-cooling capabilities, which can reduce energy consumption and improve user comfort, is still rare. Herein, we report the development of multifunctional on-skin electronics, which can passively cool human bodies without needing any energy consumption. This property is inherited from multiscale porous polystyrene-block-poly(ethylene-ran-butylene)-block-polystyrene (SEBS) supporting substrates. The multiscale pores of SEBS substrates, with characteristic sizes ranging from around 0.2 to 7 μm, can effectively backscatter sunlight to minimize heat absorption but are too small to reflect human-body midinfrared radiation to retain heat dissipation, thereby delivering around 6 °C cooling effects under a solar intensity of 840 W·m^{-2}. Other desired properties, rooted in multiscale porous SEBS substrates, include high breathability and outstanding waterproofing. The proof-of-concept bioelectronic devices include electrophysiological sensors, temperature sensors, hydration sensors, pressure sensors, and electrical stimulators, which are made via spray printing of silver nanowires on multiscale porous SEBS substrates. The devices show comparable electrical performances with conventional, rigid, nonporous ones. Also, their applications in cuffless blood pressure measurement, interactive virtual reality, and human–machine interface are demonstrated. Notably, the enabled on-skin devices are dissolvable in several organic solvents and can be recycled to reduce electronic waste and manufacturing cost. Such on-skin electronics can serve as the basis for future multifunctional smart textiles with passive-cooling functionalities.

on-skin electronics | passive cooling | breathability | waterproof | recyclability

Emerging on-skin electronics are designed to provide a noninvasive or minimally invasive way for long-term, real-time monitoring of a variety of biological signals from human bodies and can find wide applications in clinical health care, mobile fitness tracking, human–machine interface, and virtual reality among many others (1–18). To achieve their full potentials, most ongoing efforts center on developing 1) novel materials for on-skin electronics with outstanding mechanical pliability (e.g., flexible/stretchable forms of inorganic materials, intrinsically soft organic materials, nanomaterials, nanocomposites) (1, 19–22); 2) biodegradable or self-healing on-skin electronics (23–26); and 3) on-skin biochemical sensors with high stability, selectivity, and sensitivity (27–29). Besides, on-skin electronics should be breathable to facilitate sweat evaporation to improve user comfort and minimize inflammation risks (30–33), be waterproof so as not to disturb users' daily activities (e.g., showering) (34), and be reusable to potentially reduce electronic waste and manufacturing cost (35).

In addition, point-of-care thermal management (e.g., joule heating, passive cooling) shows promising applications in body temperature regulations, which can improve user comfort and reduce energy consumption. On-skin electronics with joule-heating elements have been widely reported (36–38). Also, textiles, paints, and woods with passive-cooling properties have been recently developed (39–41). Besides, very recent research reveals that twisted and coiled fibers have twistocaloric cooling capabilities, which are enabled by entropy changes at various stretching states (42). However, the studies of developing on-skin electronics, which can passively cool human bodies without needing any energy consumption, are still in the infant stage. Besides, it is worth mentioning that nanofiber-based and sugar-templated porous materials have been recently used for on-skin electronics with high breathability (30–33). However, the lack of pore size control in these porous materials constrains their capabilities in enabling on-skin electronics with passive-cooling functionalities and other desired features.

In this work, we report the development of multifunctional porous on-skin electronics, which can not only exhibit outstanding

Significance

Point-of-care thermal management (e.g., joule heating, passive cooling) shows promising applications in body temperature regulations, which can improve human comfort and reduce energy consumption. On-skin electronics with joule-heating elements have been reported. However, the research of making on-skin electronics with passive-cooling functionalities is still rare. By using multiscale porous polystyrene-block-poly(ethylene-ran-butylene)-block-polystyrene as supporting substrates, we have developed multifunctional on-skin electronics with outstanding passive-cooling capabilities, delivering around 6 °C cooling effects under a solar intensity of 840 W·m^{-2}. Other desired properties, rooted in porous SEBS substrates, include high breathability and outstanding waterproofing. In addition, a variety of bioelectronic devices are made on porous SEBS substrates via spray printing of silver nanowires (Ag NWs). The enabled devices demonstrate high performance and are recyclable.

Author contributions: Y.X., B.S., Y. Ling, G.H., and Z.Y. designed research; Y.X., B.S., Y. Ling, Q.F., Z.C., X.L., P.G., N.J., S.G., Y. Liao, S.D., Q.Y., and J.L. performed research; Y.X. and B.S. analyzed data; and Y.X., G.H., and Z.Y. wrote the paper.

The authors declare no competing interest.

This article is a PNAS Direct Submission.

[1]Y.X., B.S., and Y. Ling contributed equally to this work.

[2]To whom correspondence may be addressed. Email: huangg@missouri.edu or yanzheng@missouri.edu.

This article contains supporting information online at https://www.pnas.org/lookup/suppl/doi:10.1073/pnas.1917762116/-/DCSupplemental.

First published December 23, 2019.

passive-cooling performance but also simultaneously achieve several other attributes, such as high breathability, waterproofing, and recyclability. The unique combination of these compelling properties is rooted in multiscale porous polystyrene-block-poly(ethylene-ran-butylene)-block-polystyrene (SEBS) substrates and has not been demonstrated in state-of-the-art on-skin electronics yet. In addition, a variety of prototypic bioelectronic devices, including electrophysiological sensors, temperature sensors, hydration sensors, pressure sensors, and electrical stimulators, have been fabricated via spray printing of silver nanowires (Ag NWs) on multifunctional porous SEBS substrates. The enabled on-skin devices can perform high-fidelity measurement of various biological signals from human bodies as well as deliver electrical interventions in a programmed manner. Also, their applications in cuffless blood pressure measurement, interactive virtual reality, and human–machine interface are demonstrated.

Synthesis of Multifunctional SEBS Substrates with Multiscale Porous Structures

Phase separation-based process is simple, inexpensive, and scalable, and has been used to make porous polymeric materials for surface coatings and paints, gas storage and separation, and sound damping foams among others (39, 43). However, research on creating multiscale porous elastomeric substrates via phase separation in a controlled fashion for multifunctional on-skin electronics is still lacking. Here, we introduce the phase separation-controlled synthesis of multifunctional SEBS substrates with multiscale porous structures (Fig. 1*A* and *SI Appendix*, Fig. S1). Here, SEBS elastomer is adopted mainly due to its high stretchability and solution processability. The process starts with the preparation of a precursor solution of SEBS and isopropyl alcohol (IPA; nonsolvent) in chloroform (solvent). Next, we coat the precursor on an aluminum foil and dry it in air. The rapid evaporation of volatile chloroform (boiling point, 61.3 °C) induces the phase separation of IPA (boiling point, 82.6 °C) from SEBS to form nano/microscale droplets. Finally, the evaporation of IPA droplets leads to the formation of the SEBS substrate with hierarchical pores. The optimized porous SEBS substrate exhibits ∼70% porosity and is ∼100 μm thick, offering outstanding passive-cooling capabilities and a number of other desired properties, as discussed subsequently. The optimal thickness of the porous SEBS was obtained based

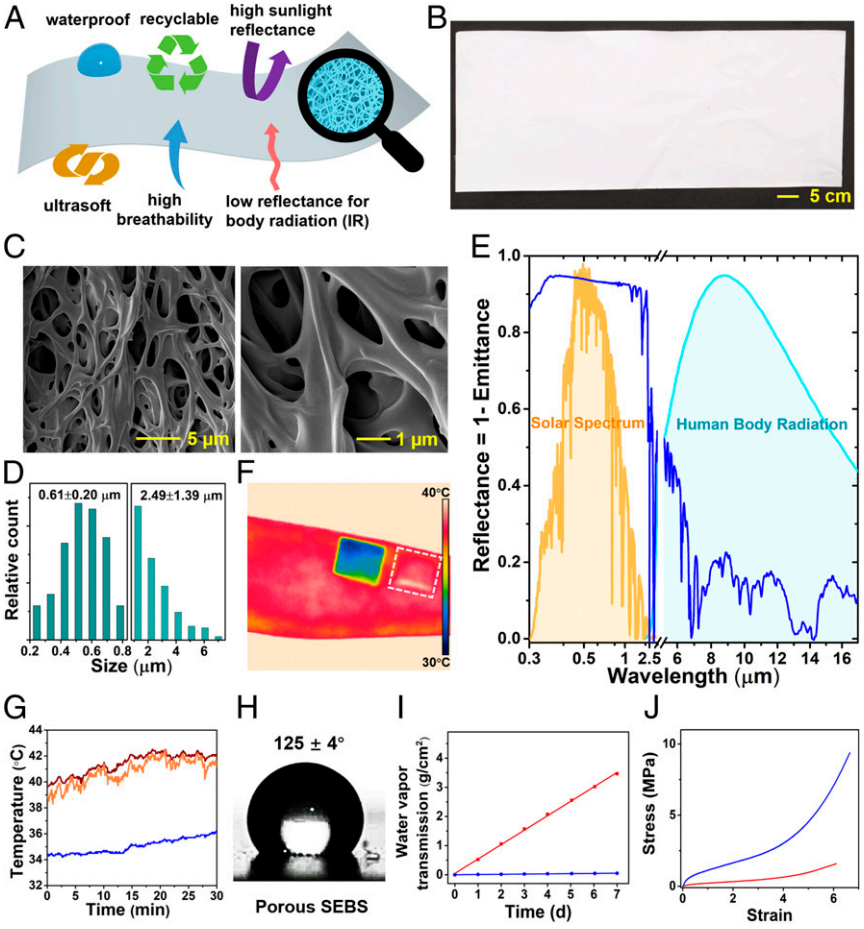

Fig. 1. Synthesis and characterizations of multifunctional SEBS substrates with multiscale porous structures. (*A*) Schematic illustrations of the multifunctional porous SEBS substrate. (*B*) A photograph of the synthesized porous SEBS substrate. (*C*) SEM images of the SEBS substrate showing the interconnected hierarchical pores. (*D*) Pore size distributions, indicating number-weighted mean pore sizes are 0.61 μm for nanopores and 2.49 μm for micropores. (*E*) Spectral reflectance of the porous SEBS substrate between 0.3 and 17 μm with a short break (5.1 to 5.2 μm). Human-body mid-IR radiation and normalized ASTM G173 Global solar spectrum are shaded as the light blue and orange regions, respectively, in *E*. Thermal mapping by IR camera (*F*) and in situ measurement of skin temperatures via thermal probe (*G*) indicate around 6 °C cooling effects induced by the porous SEBS substrate under a solar intensity of 840 $W \cdot m^{-2}$. Orange, red, and blue curves in *G*, respectively, refer to the temperatures measured from the exposed skin, skin covered with nonporous SEBS, and skin covered with porous SEBS. (*H*) Water contact angle of porous SEBS. (*I*) WVTRs of porous SEBS (red) and nonporous SEBS (blue) as a function of elapsed time. (*J*) Strain–stress curves of porous SEBS (red) and nonporous SEBS (blue).

on the trade-off of sunlight reflectance, mid-IR reflectance, and conformability with human skin (*SI Appendix*, Fig. S2).

The multiscale porous SEBS substrate indicates milky white color (Fig. 1*B*). The scanning electron microscope (SEM) images (Fig. 1*C* and *SI Appendix*, Fig. S3) show the formation of fully interconnected, hierarchical pores, with characteristic sizes ranging from around 0.2 to 7 μm. The pore size measurement, based on 300 pores, demonstrates that the number-weighted mean pore sizes are 0.61 μm for nanopores and 2.49 μm for micropores (Fig. 1*D*). As shown in Fig. 1*E*, the nano/microscale pores in the SEBS substrate can effectively backscatter sunlight (wavelength, 0.3 to 2.5 μm) but are too small to scatter human-body midinfrared (mid-IR) radiation (wavelength, 7 to 14 μm). Consequently, both a high hemispherical solar reflectance ($\bar{R}_{solar} = 0.92$ over the range of 0.3 to 2.5 μm) and a high hemispherical IR thermal emittance ($\bar{\epsilon}_{HB} = 0.85$ over the range of 7 to 14 μm) are achieved. Here, HB denotes human-body IR radiation. The calculations of $\bar{R}_{solar}$ and $\bar{\epsilon}_{HB}$ are provided in *SI Appendix*, Note S1. High $\bar{R}_{solar}$ can minimize solar heat gain, and high $\bar{\epsilon}_{HB}$ can maximize radiative heat loss. Such synergistic effects can lead to outstanding daytime passive cooling. The outdoor on-body testing shows that the skin temperature covered with porous SEBS is maintained at ∼6 °C lower than that of the exposed skin and ∼7 °C lower than that of the skin covered with nonporous SEBS after 30 and 45 min of sunlight radiation (solar intensities, 840 $W{\cdot}m^{-2}$) (Fig. 1 *F* and *G* and *SI Appendix*, Figs. S4 and S5). The cooling performance of multiscale porous SEBS is comparable to those of other passive-cooling materials, which are recently reported in the literature (*SI Appendix*, Table S1).

In addition to superior passive-cooling capabilities, the multiscale porous SEBS substrate also exhibits a number of other desired features for on-skin electronics, including waterproofing, high breathability, recyclability, low elastic modulus, low mass density, high stretchability, and conformability. First, multiscale porous SEBS indicates enhanced hydrophobicity (water contact angle, 125 ± 4°; Fig. 1*H*) compared to nonporous SEBS (water contact angle, 94 ± 2°; *SI Appendix*, Fig. S6), mainly due to increased surface roughness stemming from porous structures. As illustrated in *SI Appendix*, Fig. S7, multiscale porous SEBS exhibits outstanding waterproof capability because of its high hydrophobicity as well as conformal contact with skin, which is further confirmed by the on-body device testing in water. Second, as shown in Fig. 1*I*, porous SEBS shows a high water vapor transmission rate (WVTR) (0.0206 $g{\cdot}cm^{-2}{\cdot}h^{-1}$) due to the interconnected hierarchical pores, which is about 69 times higher than that of nonporous SEBS with the same thickness and is comparable to recently developed, passive cooling, nanoPE fabrics (0.023 $g{\cdot}cm^{-2}{\cdot}h^{-1}$) (44). The high WVTR can expedite perspiration evaporation to improve user comfort as well as minimize inflammatory reactions caused by sweat accumulation. Third, the introduction of porous structures in the SEBS substrate can reduce the mass occupation and also create sufficient localized empty space to reduce the effective elastic modulus. Thus, the obtained porous SEBS substrate is ultrasoft and lightweight (Fig. 1*J*). Its modulus (∼0.2 MPa) and mass density (∼0.25 g/cm^3) are comparable to epidermis (modulus, 0.14 to 0.6 MPa; density, ∼1.05 g/cm^3) and smaller than the data measured from nonporous SEBS (modulus, ∼1.1 MPa; density, ∼0.89 g/cm^3). The low elastic modulus can avoid skin irritation, improve user comfort, and also facilitate the formation of conformal contact with skin. The low mass density can enable lightweight on-skin electronics to alleviate physical constraints exerted on human bodies. Also, the multiscale porous SEBS substrate is highly stretchable (∼600%). Besides, the enabled on-skin devices are recyclable, which is demonstrated subsequently.

Spray Printing of Ag NWs on Prestretched Multiscale Porous SEBS Substrates

Ideally, on-skin electronics should be one-time use and disposable to minimize infection risks. Thus, it is highly desirable to achieve scalable patterning of electronic components on supporting substrates to potentially lower manufacturing cost. The solution-printing–based fabrication offers a simple, cost-effective, high-throughput way for patterning devices on flexible supporting substrates (5, 45, 46). In this research, we fabricated a variety of prototypic on-skin bioelectronic devices via spray printing of Ag NWs on multiscale porous SEBS substrates. Here, Ag NWs (diameter, 50 nm; length, 100 to 200 μm) are used mainly because they exhibit outstanding mechanical compliance and high electrical conductivity, and can be easily produced in a large quantity (37).

As illustrated in Fig. 2 *A* and *B*, we first investigate the spray printing of open-mesh, serpentine-like layouts of Ag NWs on prestretched multiscale porous SEBS (uniaxial prestrain, 150%), which can serve as the basic building blocks for a variety of bioelectronic devices as demonstrated in Fig. 3. After the spray printing, releasing the prestretched substrate leads to the formation of microscale wavy structures of Ag NWs networks with underneath porous SEBS (Fig. 2*C* and *SI Appendix*, Fig. S8). The spray-printed Ag NWs patterns (∼200 nm thick) show high electrical conductivity (11,000 S/cm). Also, the wavy structures endow the printed Ag NWs with outstanding electromechanical properties. For example, both bending and stretching produce small effects on their electrical properties (Fig. 2 *D* and *E*). In particular, the electrical resistance shows a negligible change (∼1%) at a bending radius of 1 mm and increases ∼17% under 100% uniaxial strain. By contrast, the natural deformations of human skin are up to 50 to 80%. Also, the spray-printed Ag NWs exhibit high durability and cyclability (*SI Appendix*, Fig. S9). After 1,000 cycles for a bending radius of 1 mm, the resistance only increases ∼1.7%. Similarly, only ∼6% resistance increase is observed after 2,000 cycles of stretching test under 50% uniaxial strain.

Most importantly, the integration of open-mesh, serpentine-like patterns of Ag NWs exhibits negligible effects on the passive-cooling capability, breathability, and elastic modulus of multiscale porous SEBS substrates (Fig. 2*F*). This is largely because porous SEBS is the major component of the obtained sample. Specifically, the Ag NWs patterns only occupy ∼1% by weight and ∼0.2% by thickness of the entire sample and account for ∼16% surface coverage on the side that directly touches the skin. It is worth noting that Ag NWs can not only reflect IR radiation to warm human body but also enhance the surface emissivity to efficiently dissipate heat back to the environment (47, 48). The coating of Ag NWs serpentine patterns has a trivial effect on the cooling performance of porous SEBS, indicating ∼6 °C and ∼6.3 °C temperature drops, respectively, before and after Ag NWs printing. This is mainly because 1) Ag NWs patterns only occupy a small portion of the surface area of the sample (∼16%); and 2) Ag NWs are outstanding thermal conductors, which can enable efficient heat transfer between skin and multiscale porous SEBS (*SI Appendix*, Fig. S10). In addition, the obtained sample can form robust, conformal contact with the skin (Fig. 2*G*) mainly due to its low effective modulus (∼0.2 MPa) and small thickness (∼100 μm). As shown in *SI Appendix*, Fig. S11, adhesion peel test indicates porous SEBS exhibits a significantly higher skin adhesion force than that of its nonporous counterpart with the same thickness, which is comparable to the data measured from ultrathin epidermal electronic systems (49).

Multimodal On-Skin Electronics Based on Multiscale Porous SEBS and Spray-Printed Ag NWs

Human bodies usually undergo complex physiological changes in daily activities and can naturally emanate a broad spectrum of

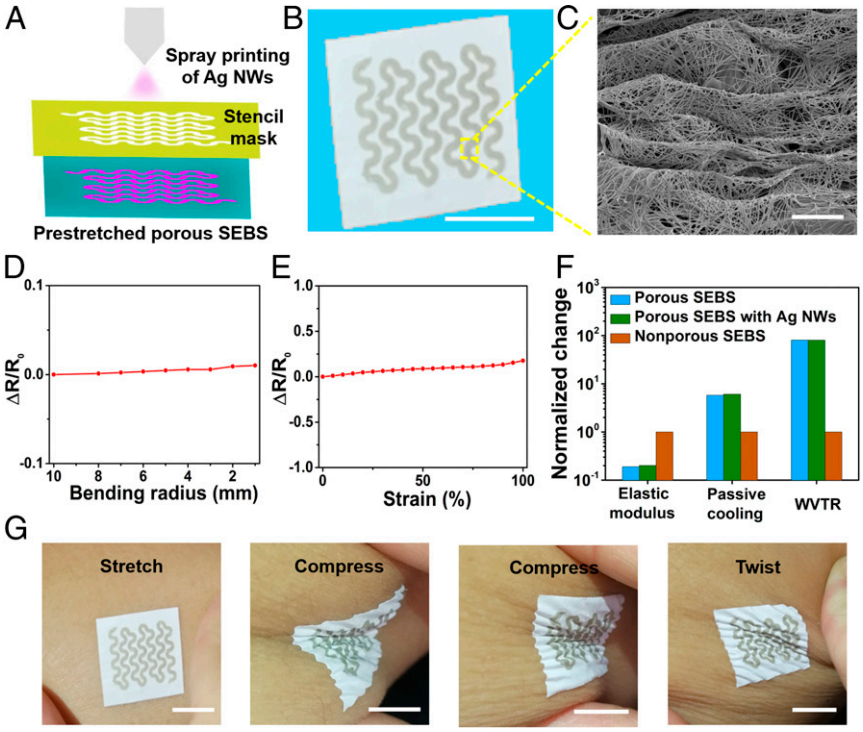

Fig. 2. Spray printing of Ag NW-based on-skin electronics on multiscale porous SEBS substrates. (*A*) A schematic diagram of the spray printing of Ag NWs onto prestretched porous SEBS through a stencil mask. (*B*) A photograph of a serpentine-like conductive trace, made of spray-printed Ag NWs, on porous SEBS. (Scale bar: 1 cm.) (*C*) SEM image, showing the formation of microscale wavy structures of Ag NWs networks with underneath porous SEBS. (Scale bar: 5 μm.) Variations in electrical resistance of the Ag NWs patterns on porous SEBS as a function of bending radius (*D*) and strain (*E*). (*F*) Comparisons of nonporous SEBS, porous SEBS, and porous SEBS with Ag NWs patterns, in terms of water vapor transmission rate (WVTR), passive-cooling capability, and elastic modulus, indicating significant improvement of porous SEBS over nonporous SEBS and negligible changes after Ag NW printing. (*G*) Photographs, showing the formation of the robust conformal contact between the sample and the skin. Mechanical deformations, including stretching, compressing, and twisting, do not induce delamination. (Scale bars: 1 cm.)

biological information. Thus, it is highly desirable to enable on-skin electronics with multimodalities (i.e., incorporate multiple sensors and stimulators together) to obtain a complete picture of the body's physiological status as well as deliver required interventions. Here, we demonstrate porous, multimodal on-skin bioelectronic patches, consisting of electrophysiological (i.e., biopotential) sensors, temperature sensors, hydration sensors, and electrical stimulators (Fig. 3*A* and *SI Appendix*, Fig. S12), which are fabricated via spray printing of Ag NWs on multiscale porous SEBS substrates. The enabled porous on-skin devices show comparable electrical performances with conventional, rigid, nonporous ones, as described below.

The electrophysiological sensor consists of reference, ground, and measurement electrodes of Ag NWs. As shown in Fig. 3*B* and *SI Appendix*, Figs. S13–S19, the obtained on-skin electrophysiological sensor can be laminated onto the different locations of human bodies to record alpha rhythm (from forehead), electrocardiograms (ECGs) (from chest), and electromyograms (EMGs) (from forearm, flexor carpi radialis muscle; face, masseter muscle; and back and neck, trapezius muscle). The contact impedance is ∼33 kΩ at 100 Hz, comparable to conventional silver/silver chloride (Ag/AgCl) gel electrodes (∼21 kΩ at 100 Hz). (*SI Appendix*, Fig. S20). Both ECGs and EMGs recorded using the porous on-skin sensors exhibit quantitively comparable patterns with those measured by Ag/AgCl gel electrodes (*SI Appendix*, Fig. S16). Specifically, the EMGs recorded with the porous on-skin devices indicate the signal-to-noise ratio (SNR) of ∼20.7 dB. As a comparison, the SNR of the EMGs measured with Ag/AgCl electrodes is ∼22.4 dB. Besides, the device fabrication process reported in this research is highly reproducible, as confirmed by the highly repeatable ECGs recording from 8 randomly selected devices (*SI Appendix*, Fig. S17). Also, the long-term and continuous ECG measurement (*SI Appendix*, Fig. S18) indicates the high device stability. In addition, due to the porous structures of enabled on-skin devices, the heavy skin perspiration and high levels of moisture have the trivial effects on the device performance (*SI Appendix*, Fig. S19).

It is known that electrical stimulations can alleviate pain and are also useful for rehabilitation and prosthetic motor control (50, 51). As shown in Fig. 3*C*, monophasic square pulses of 2 mA (10 Hz; pulse duration, 25 ms) is applied through the bipolar stimulation electrodes of Ag NWs to the forearm. The recorded EMG signals, from the muscle (flexor carpi radialis) contractions induced by the electrical stimulations, exhibit a good alignment with the stimulation signals, indicating the capability of delivering required electrical interventions in a programmed manner.

Furthermore, we demonstrate the application of the enabled on-skin electrophysiological sensors in the control of a soft robotic hand, which is based on graphene electrothermal actuators. Specifically, 2 on-skin electrophysiological sensor patches were laminated, respectively, on the extensor pollicis longus and extensor pollicis brevis muscles, and flexor carpi radialis muscle of a human volunteer to record EMGs. The EMG signals acquired from the extensor pollicis longus and extensor pollicis brevis muscles were used to control the soft robotic thumb, whereas the EMG signals recorded from the flexor carpi radialis muscle were used to control another 4 fingers. As shown in Fig. 3*D* and Movie S1, the soft robotic hand can successfully identify and emulate human hand motions. The response time is ∼8 s, the bending angle is ∼360°, and the bending curvature is ∼1.4 cm^{-1}.

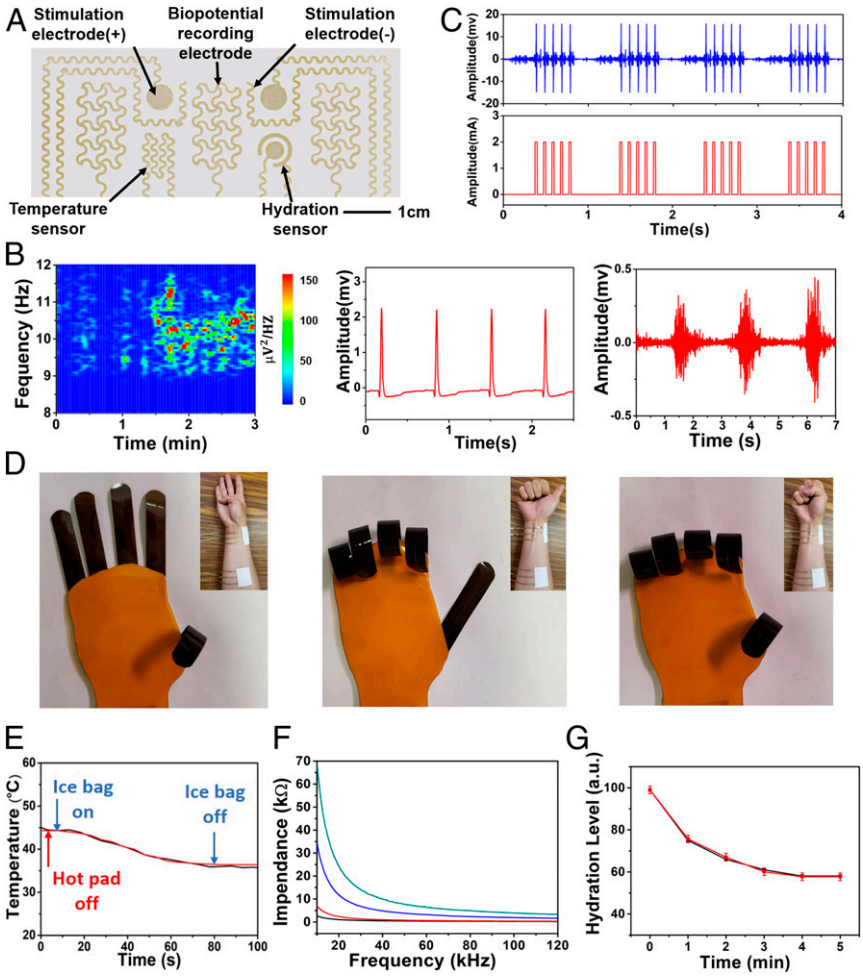

Fig. 3. Multimodal on-skin electronics based on multiscale porous SEBS and spray-printed Ag NWs. (*A*) A photograph of the multimodal on-skin electronic patch, which was fabricated via the spray printing of Ag NWs on the multifunctional porous SEBS substrate. (*B*) Recorded alpha rhythm (*Left*), ECG signals (*Middle*), and EMG signals (*Right*). (*C*) Recorded EMG signals (*Top*) during electrical stimulations (*Bottom*). (*D*) Photographs, indicating the control of a soft robotic hand via EMGs recording. (*E*) Recorded skin temperatures (blue), which nearly overlaps with the data measured from a thermocouple (red). Here, a hot pad was applied to warm the skin to ∼45 °C before the test. Then an ice bag was used to accelerate cooling during the test. (*F*) Impedance variations as a function of frequency at the hydration levels of 99% (green), 88% (blue), 70% (red), and 67% (black). (*G*) Recorded skin hydration decay as a function of time after applying moisturizing lotion (red), which agrees well with the data measured from a commercial skin moisture sensor (black).

In addition, the enabled on-skin temperature sensors and hydration sensors also demonstrate high performance (Fig. 3 *E*–*G*). The on-skin temperature sensor consists of an Ag NW conductive trace. The temperature coefficient of resistance is 2.14×10^{-3} °C^{-1} (*SI Appendix*, Fig. S21) and provides the basis for the on-skin thermal measurement. Here, a hot pad was applied to warm the skin to ∼45 °C before the test. Then an ice bag was used to accelerate cooling during the test. Fig. 3*E* indicates that the skin temperatures measured using the on-skin temperature sensor nearly overlap with the ones recorded with a commercial thermocouple. The on-skin hydration sensor consists of a coaxial dot-ring electrode of Ag NWs and can measure skin impedance, reflecting skin hydration levels. Fig. 3*F* shows the skin impedance variations as a function of frequency at different hydration levels, indicating the correlations between skin impedance and hydration levels. The on-skin hydration sensor was calibrated using a commercial skin moisture sensor and was used to examine the natural decay of skin hydration levels after applying moisturizing lotion. The results recorded by the on-skin hydration sensor agree well with the data obtained from a commercial hydration sensor (Fig. 3*G*). The calculated SD is 1.8% based on a sample size of 16.

Demonstrations of Waterproof, Recyclability, and Cuffless Blood Pressure Measurement

As demonstrated in Fig. 4*A*, *SI Appendix*, Fig. S22, and Movie S2, the enabled on-skin electronic patch is waterproof and can operate well in water. During the testing, the volunteer was asked to wear the on-skin device on the forearm and then fully submerged the forearm in water. After 20 min, the volunteer was asked to squeeze the fist in water once, twice, 3 times, 4 times, and 5 times. Remarkably, the recorded EMG signals are clearly distinguishable from the baseline noise and are comparable to the data recorded in air. Moreover, our on-skin electronics based on multiscale porous SEBS substrates and Ag NWs are recyclable. By contrast, silicone elastomer (e.g., polydimethylsiloxane), one widely used substrate material for on-skin electronics, is not dissolvable after curing and thus is not recyclable. As shown in *SI Appendix*, Fig. S23*A*, we can dissolve the obtained multifunctional on-skin electronic patch in chloroform and then separate SEBS with Ag NWs via centrifugation for reuse. Details on the recyclable process are provided in *SI Appendix*, Note S2. The porous on-skin devices made of reused SEBS and Ag NWs exhibit comparable performances with the ones made of fresh materials (*SI Appendix*, Fig. S23*B*).

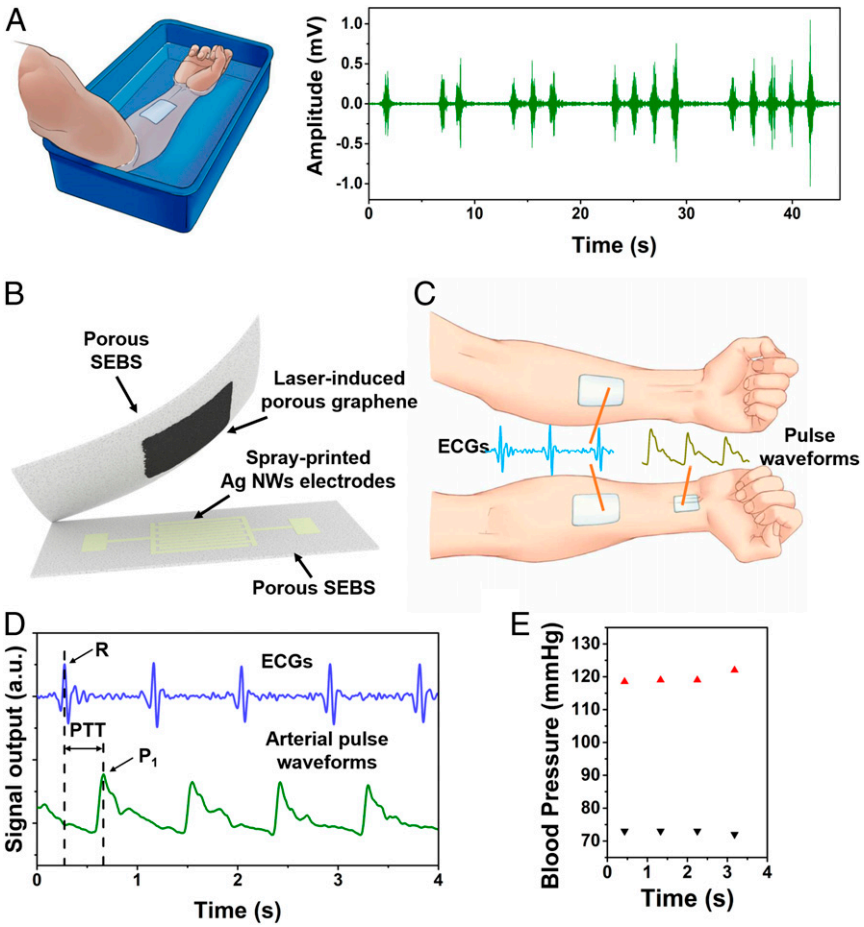

Fig. 4. Demonstrations of waterproofing and continuous cuffless blood pressure measurement. (*A*) EMGs recording when the on-skin device was fully submerged in water. (*B*) A schematic diagram of the assembled piezoresistive on-skin pressure sensor. (*C*) Schematic illustrations of the simultaneous recording of ECG signals and arterial pulse waveforms for blood pressure monitoring. (*D*) Recorded concurrent ECG signals and arterial pulse waveforms with the pulse transit time (PTT) indicated. (*E*) The calculated beat-to-beat systolic blood pressures (red) and diastolic blood pressures (black) based on the PTT method.

Continuous cuffless monitoring of blood pressures can provide a wealth of information for the quantitative evaluation of various cardiovascular diseases as well as general health (52–54). In this research, we demonstrate the application of multiscale porous SEBS-based on-skin devices in continuous cuffless measurement of beat-to-beat blood pressures via concurrent recording of ECGs and arterial pulse waveforms (Fig. 4 *B–D*). The ECG measurement was performed using the aforementioned porous on-skin electrophysiological sensors. The pulse waveforms monitoring was conducted with a piezoresistive on-skin pressure sensors, consisting of laser-induced porous graphene (55) as sensing elements, a pair of interdigital electrodes of spray-printed Ag NWs, and top encapsulation and bottom supporting layers of multiscale porous SEBS (Fig. 4*B*). As demonstrated in *SI Appendix*, Fig. S24, the assembled pressure sensor indicates high sensitivity, high repeatability, and quick response time (~36 ms). For instance, it can monitor a minute pressure change caused by the stepwise addition of a 10-μL water droplet and exhibits negligible change after repetitive pressure loading for 1,000 cycles.

As illustrated in Fig. 4*C*, the continuous, simultaneous recording of ECGs and pulse waveforms was conducted by applying 2 on-skin electrophysiological sensors on the forearms and one on-skin pressure sensor on the wrist. The obtained results are provided in Fig. 4*D*. The beat-to-beat diastolic blood pressures and systolic blood pressures are extracted using a pulse transit time (PTT) method (Fig. 4*E*) (56). The PTT is the time interval between the "R" peak of the ECG signal and the P_1 point of the pulse waveform within the same cardiac cycle (Fig. 4*D*). Details on the correlation between blood pressures and the PTT are provided in *SI Appendix*, Note S3. Notably, the measured beat-to-beat diastolic blood pressures and systolic blood pressures using our porous on-skin devices are in good agreement with the results measured from a commercial sphygmomanometer (*SI Appendix*, Fig. S25).

Control of a Virtual Character and a Quadcopter via Real-Time EMGs Recording

Furthermore, we demonstrate the applications of the enabled porous on-skin electronics in interactive virtual reality and real-time control of a quadcopter via high-fidelity EMG recording. The flowchart is provided in *SI Appendix*, Fig. S26. Specifically, the on-skin EMG sensors are laminated on the forearms (muscle, flexor carpi radialis) to collect the relevant EMG signals when the volunteers perform 4 different bimanual gestures: bending wrists inward, bending wrists to the left, bending wrists to the right, and bending wrists outward. As shown in Fig. 5*A*, the root-mean-square (RMS) values of the recorded EMG signals exhibit characteristic patterns and can be classified into 4 distinct control signals, termed A, B, C, and D. Details on RMS calculations and signal classifications are provided in *SI Appendix*, Note S4. The classification accuracy is evaluated and summarized in a confusion matrix (Fig. 5*B*), where the columns and rows represent actual gestures and predicated signals, respectively. Each bimanual gesture was repeated 50 times. The success rates are 94%, 92%,

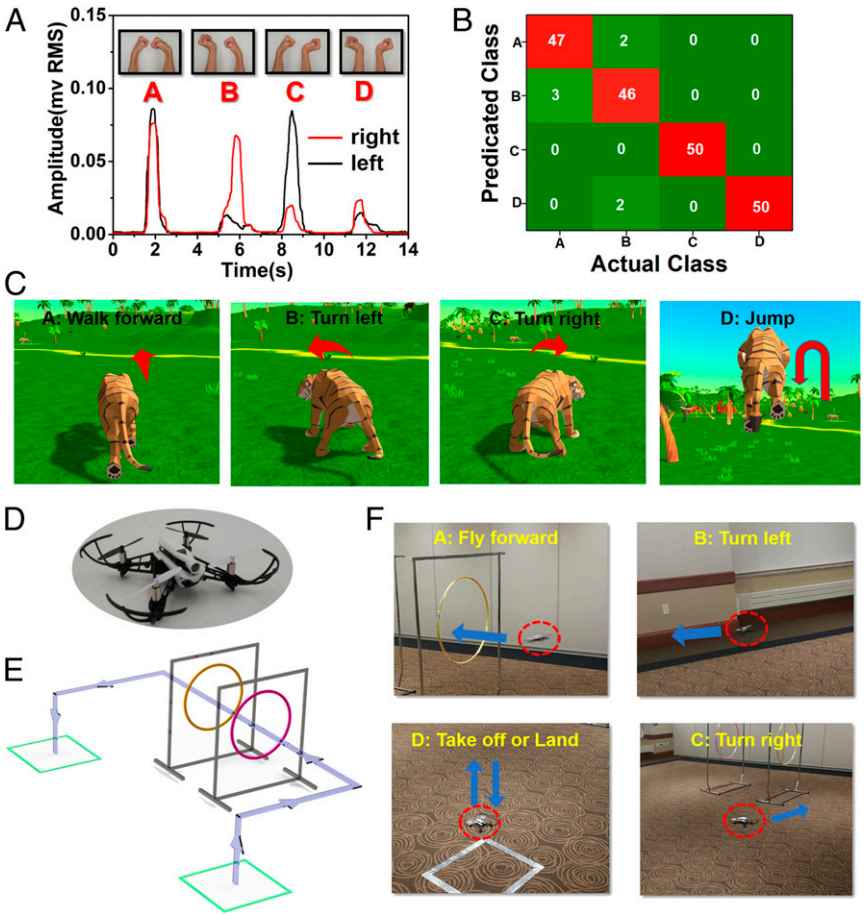

Fig. 5. Control of a virtual character and a quadcopter via real-time EMG recording. (*A*) EMG signals recorded from the forearms associated with 4 different bimanual gestures (*Inset*), which can be classified into 4 distinct control signals, termed A, B, C, and D. (*B*) Confusion matrix that indicates the classification accuracy. Each bimanual gesture was repeated 50 times. The columns and rows represent actual gestures (actual class) and predicted signals (predicated class), respectively. Numbers are highlighted in the box to show the distribution of predicted signals in each actual gesture motion. (*C*) Control of a virtual tiger in a 3D game engine using bimanual gestures, where A, B, C, and D correspond to "walk forward," "turn left," "turn right," and "jump," respectively. (*D*) A photograph of the quadcopter used in the research. (*E*) Schematic illustrations of the quadcopter trajectory controlled by bimanual gestures, where arrows indicate the flying direction. (*F*) Images of the quadcopter control by bimanual gestures, where A, B, C, and D correspond to "fly forward," "turn left," "turn right," and "take off or land," respectively.

100%, and 100% for the predicted signals of A, B, C, and D, respectively. The overall accuracy is 96.5%.

The high-fidelity EMGs recording and high classification accuracy can enable the real-time, high-precision control of a virtual character and a quadcopter using human bimanual gestures. As shown in Fig. 5*C* and Movie S3, the control of a virtual tiger in a 3D game engine is realized using bimanual gestures. Here, A, B, C, and D correspond to "walk forward," "turn left," "turn right," and "jump," respectively. The quadcopter used in the research is shown in Fig. 5*D*. Four bimanual gestures are assigned to 5 different quadcopter control commands: A, "fly forward"; B, "turn left"; C, "turn right"; first D, "take off"; and second D, "land." As demonstrated in Fig. 5 *D* and *E* and Movie S4, the bimanual gestures can precisely control the motion and trajectory of the quadcopter in a real-time and wireless manner.

Conclusion

In summary, we report the synthesis of multiscale porous SEBS substrates and their applications in multifunctional on-skin electronics with passive-cooling capabilities. In addition to passive cooling, the enabled on-skin devices exhibit a collection of other compelling features, such as high breathability, waterproofing, and recyclability. On-skin electronics with the unique combination of these desired features have not been achieved yet. In this research, we demonstrate the applications of the enabled on-skin devices in 1) high-fidelity monitoring of biopotentials, body temperatures, skin hydration levels, pulse waveforms, and blood pressures; 2) efficient administration of programmed electrical interventions; and 3) high-precision control of a soft robotic hand, a virtual character, and a quadcopter. In addition, the reported fabrication approaches, for both the synthesis of multiscale porous SEBS substrates and printing of bioelectronic devices, are simple, inexpensive, and scalable, which can facilitate the high-throughput manufacturing and practical applications.

Materials and Methods

Synthesis of Multiscale Porous SEBS Substrates. Commercially available SEBS powders (H1062; Asahi Kasei) were first dissolved in chloroform to prepare the SEBS stock solution (60 mg·mL^{-1}). Next, the precursor solution was prepared by mixing the stock solution with isopropyl alcohol at a volume ratio of 5:2, followed by sonication for 30 min. Dropcasting the resulting solution on an aluminum foil and drying the sample under ambient conditions completed the synthesis of the multifunctional SEBS substrate with multiscale porous structures.

Spray Printing of Ag NWs-Based On-Skin Electronics on Prestretched Multiscale Porous SEBS Substrates. Commercially available Ag NWs (Ag NW-L50; ACS Material) were diluted to ~2 mg·mL^{-1} in ethanol and then spray-printed onto the prestretched multiscale porous SEBS substrate (prestrain, 150%) through a stencil mask using a commercial airbrush (G222; Master Airbrush).

The spray-printing process was carried out under ambient conditions with a nozzle to the substrate distance of ∼10 cm and airbrush pressure of ∼20 psi. Next, the stencil mask was removed and the prestretched multiscale porous SEBS substrate was released to the original state. Rinsing the sample in water and ethanol and drying at 60 °C for 30 min in air completed the device fabrication.

Characterizations and Measurements. SEM images were taken with a FEI Quanta 600 FEG Environmental SEM. Spectral reflectance of the obtained porous SEBS substrates in the sunlight and mid-IR ranges was examined, respectively, using a UV/Vis/NIR spectrophotometer (Perkin-Elmer Lambda 1050; PerkinElmer) with a 150-mm integrating sphere and a Fourier transform IR spectrometer (Nicolet 6700; Thermo Electron Corporation) with a gold integrating sphere. Solar intensity was measured with a solar power meter (TES-132; TES Electrical Electronic Corporation). Skin temperatures in Fig. 1*G* were recorded using the thermocouples (SA1-K; OMEGA Engineering) with a thermometer (HH309A; OMEGA Engineering). Fig. 1*F* was taken with a commercial thermal camera (FLIR E6). WVTR test was conducted at 35 °C based on ASTME96. Water contact angles were measured with a video contact angle system (VCA 2500XE; AST Products). Electromechanical properties were measured with Mark-10 ESM303 tensile tester together with a digital source meter (2604B; Keithley Instruments).

Electrophysiological signals were measured using PowerLab T26 (AD Instruments). Both the impedance variations of the on-skin hydration sensors and resistance change of the on-skin temperature sensors were recorded with LCR meter (IM3523; HIOKI). The on-skin hydration sensor was calibrated with a commercial hydrometer (Moritex Moist Sense II; Moritex Corporation). Electrical stimulations (pulse duration, 25 ms; current, 2 mA) were delivered by a digital source meter (Keithley 2604B). PowerLab T26 was used to concurrently record ECG signals and pulse waveforms for blood pressure measurement. The results were compared to the blood pressures measured with a commercial sphygmomanometer (BP653; Omron). Tiger simulator 3D video game (Cyber Goldfinch) was used for the interactive virtual reality demonstration. A quadcopter (Parrot Mambo FPV) was wirelessly controlled by Python script, which acquired commands from Matlab-classified EMG signals. In this research, flexible anisotropic conductive film cables were used to connect the obtained devices with external data acquisition systems.

Experiments on Human Subjects. The on-body evaluations of the on-skin electronic devices were conducted under approval from the Institutional Review Board at the University of Missouri–Columbia (Project 2010272). All human subjects gave written, informed consent before participation in the study.

Data and Materials Availability. All data needed to evaluate the conclusions in the paper are present in the paper, *SI Appendix*, and Movies S1–S4.

ACKNOWLEDGMENTS. Z.Y. acknowledges financial support from the University of Missouri–Columbia start-up fund. G.H. acknowledges support from the Air Force Office of Scientific Research under Grant AF 9550-18-1-0342 with Dr. Byung-Lip (Les) Lee, the program manager. P.G. and N.J. were supported by Laboratory Directed Research and Development (LDRD) funding from Argonne National Laboratory, provided by the Director, Office of Science, US Department of Energy under Contract No. DE-AC02-06CH11357.

1. D.-H. Kim *et al*., Epidermal electronics. *Science* **333**, 838–843 (2011).
2. T. R. Ray *et al*., Bio-integrated wearable systems: A comprehensive review. *Chem. Rev.* **119**, 5461–5533 (2019).
3. T. Someya, M. Amagai, Toward a new generation of smart skins. *Nat. Biotechnol.* **37**, 382–388 (2019).
4. A. Chortos, J. Liu, Z. Bao, Pursuing prosthetic electronic skin. *Nat. Mater.* **15**, 937–950 (2016).
5. T. Someya, Z. Bao, G. G. Malliaras, The rise of plastic bioelectronics. *Nature* **540**, 379–385 (2016).
6. W. Gao, H. Ota, D. Kiriya, K. Takei, A. Javey, Flexible electronics toward wearable sensing. *Acc. Chem. Res.* **52**, 523–533 (2019).
7. K. Sim, Z. Rao, F. Ershad, C. Yu, Rubbery electronics fully made of stretchable elastomeric electronic materials. *Adv. Mater.*, 10.1002/adma.201902417 (2019).
8. C. Choi, Y. Lee, K. W. Cho, J. H. Koo, D.-H. Kim, Wearable and implantable soft bioelectronics using two-dimensional materials. *Acc. Chem. Res.* **52**, 73–81 (2019).
9. E. J. Markvicka, M. D. Bartlett, X. Huang, C. Majidi, An autonomously electrically self-healing liquid metal-elastomer composite for robust soft-matter robotics and electronics. *Nat. Mater.* **17**, 618–624 (2018).
10. G. S. C. Bermúdez, H. Fuchs, L. Bischoff, J. Fassbender, D. Makarov, Electronic-skin compasses for geomagnetic field-driven artificial magnetoreception and interactive electronics. *Nat. Electron.* **1**, 589–595 (2018).
11. B. Yin, X. Liu, H. Gao, T. Fu, J. Yao, Bioinspired and bristled microparticles for ultrasensitive pressure and strain sensors. *Nat. Commun.* **9**, 5161 (2018).
12. S. Hong *et al*., Wearable thermoelectrics for personalized thermoregulation. *Sci. Adv.* **5**, eaaw0536 (2019).
13. K. Sim *et al*., Three-dimensional curvy electronics created using conformal additive stamp printing. *Nat. Electron.*, **2**, 471–479 (2019).
14. K. Sim *et al*., Metal oxide semiconductor nanomembrane-based soft unnoticeable multifunctional electronics for wearable human-machine interfaces. *Sci. Adv.* **5**, eaav9653 (2019).
15. S. Yang *et al*., "Cut-and-paste" manufacture of multiparametric epidermal sensor systems. *Adv. Mater.* **27**, 6423–6430 (2015).
16. S. Kabiri Ameri *et al*., Graphene electronic tattoo sensors. *ACS Nano* **11**, 7634–7641 (2017).
17. Z. Xue, H. Song, J. A. Rogers, Y. Zhang, Y. Huang, Mechanically-guided structural designs in stretchable inorganic electronics. *Adv. Mater.* 10.1002/adma.201902254 (2019).
18. G. Chen *et al*., Plasticizing silk protein for on-skin stretchable electrodes. *Adv. Mater.* **30**, e1800129 (2018).
19. J. Y. Oh *et al*., Intrinsically stretchable and healable semiconducting polymer for organic transistors. *Nature* **539**, 411–415 (2016).
20. S. Wang *et al*., Skin electronics from scalable fabrication of an intrinsically stretchable transistor array. *Nature* **555**, 83–88 (2018).
21. H.-J. Kim, K. Sim, A. Thukral, C. Yu, Rubbery electronics and sensors from intrinsically stretchable elastomeric composites of semiconductors and conductors. *Sci. Adv.* **3**, e1701114 (2017).
22. X. Cheng, Y. Zhang, Micro/nanoscale 3D assembly by rolling, folding, curving, and buckling approaches. *Adv. Mater.* **31**, e1901895 (2019).
23. D. Son *et al*., An integrated self-healable electronic skin system fabricated via dynamic reconstruction of a nanostructured conducting network. *Nat. Nanotechnol.* **13**, 1057–1065 (2018).
24. B. C. Tee, C. Wang, R. Allen, Z. Bao, An electrically and mechanically self-healing composite with pressure- and flexion-sensitive properties for electronic skin applications. *Nat. Nanotechnol.* **7**, 825–832 (2012).
25. C. M. Boutry *et al*., A sensitive and biodegradable pressure sensor array for cardiovascular monitoring. *Adv. Mater.* **27**, 6954–6961 (2015).
26. T. Lei *et al*., Biocompatible and totally disintegrable semiconducting polymer for ultrathin and ultralightweight transient electronics. *Proc. Natl. Acad. Sci. U.S.A.* **114**, 5107–5112 (2017).
27. W. Gao *et al*., Fully integrated wearable sensor arrays for multiplexed in situ perspiration analysis. *Nature* **529**, 509–514 (2016).
28. M. Bariya, H. Y. Y. Nyein, A. Javey, Wearable sweat sensors. *Nat. Electron.* **1**, 160–171 (2018).
29. T. Wang *et al*., Tactile chemomechanical transduction based on an elastic microstructured array to enhance the sensitivity of portable biosensors. *Adv. Mater.* **31**, e1803883 (2019).
30. Z. Jiang *et al*., Highly stretchable metallic nanowire networks reinforced by the underlying randomly distributed elastic polymer nanofibers via interfacial adhesion improvement. *Adv. Mater.* **31**, e1903446 (2019).
31. A. Miyamoto *et al*., Inflammation-free, gas-permeable, lightweight, stretchable on-skin electronics with nanomeshes. *Nat. Nanotechnol.* **12**, 907–913 (2017).
32. H. Jin *et al*., Highly durable nanofiber-reinforced elastic conductors for skin-tight electronic textiles. *ACS Nano* **13**, 7905–7912 (2019).
33. B. Sun *et al*., Gas-permeable, multifunctional on-skin electronics based on laser-induced porous graphene and sugar-templated elastomer sponges. *Adv. Mater.* **30**, e1804327 (2018).
34. J.T. Reeder *et al*., Waterproof, electronics-enabled, epidermal microfluidic devices for sweat collection, biomarker analysis, and thermography in aquatic settings. *Sci. Adv.* **5**, eaau6356 (2019).
35. Z. Zou *et al*., Rehealable, fully recyclable, and malleable electronic skin enabled by dynamic covalent thermoset nanocomposite. *Sci. Adv.* **4**, eaaq0508 (2018).
36. S. Choi *et al*., Stretchable heater using ligand-exchanged silver nanowire nanocomposite for wearable articular thermotherapy. *ACS Nano* **9**, 6626–6633 (2015).
37. S. Choi *et al*., Highly conductive, stretchable and biocompatible Ag-Au core-sheath nanowire composite for wearable and implantable bioelectronics. *Nat. Nanotechnol.* **13**, 1048–1056 (2018).
38. A. Hazarika *et al*., Woven Kevlar fiber/polydimethylsiloxane/reduced graphene oxide composite-based personal thermal management with freestanding Cu-Ni core-shell nanowires. *Nano Lett.* **18**, 6731–6739 (2018).
39. J. Mandal *et al*., Hierarchically porous polymer coatings for highly efficient passive daytime radiative cooling. *Science* **362**, 315–319 (2018).
40. P.-C. Hsu *et al*., Radiative human body cooling by nanoporous polyethylene textile. *Science* **353**, 1019–1023 (2016).
41. T. Li *et al*., A radiative cooling structural material. *Science* **364**, 760–763 (2019).
42. R. Wang *et al*., Torsional refrigeration by twisted, coiled, and supercoiled fibers. *Science* **366**, 216–221 (2019).
43. F. Wang *et al*., Progress report on phase separation in polymer solutions. *Adv. Mater.* **31**, e1806733 (2019).
44. Y. Peng *et al*., Nanoporous polyethylene microfibres for large-scale radiative cooling fabric. *Nat. Sustain.* **1**, 105–112 (2018).
45. N. Matsuhisa *et al*., Printable elastic conductors by in situ formation of silver nanoparticles from silver flakes. *Nat. Mater.* **16**, 834–840 (2017).

46. A. G. Kelly *et al*., All-printed thin-film transistors from networks of liquid-exfoliated nanosheets. *Science* **356**, 69–73 (2017).
47. P. C. Hsu *et al*., Personal thermal management by metallic nanowire-coated textile. *Nano Lett.* **15**, 365–371 (2015).
48. N. N. Shi *et al*., Thermal physiology. Keeping cool: Enhanced optical reflection and radiative heat dissipation in Saharan silver ants. *Science* **349**, 298–301 (2015).
49. H.U. Chung *et al*., Binodal, wireless epidermal electronic systems with in-sensor analytics for neonatal intensive care. *Science* **363**, eaau0780 (2019).
50. P. Sarzi-Puttini *et al*., *Seminars in Arthritis and Rheumatism* (Elsevier, 2005), vol. 35, pp. 1–10.
51. B. Xu *et al*., An epidermal stimulation and sensing platform for sensorimotor prosthetic control, management of lower back exertion, and electrical muscle activation. *Adv. Mater.* **28**, 4462–4471 (2016).
52. Y. Ma *et al*., Relation between blood pressure and pulse wave velocity for human arteries. *Proc. Natl. Acad. Sci. U.S.A.* **115**, 11144–11149 (2018).
53. N. Luo *et al*., Flexible piezoresistive sensor patch enabling ultralow power cuffless blood pressure measurement. *Adv. Funct. Mater.* **26**, 1178–1187 (2016).
54. K. Meng *et al*., Flexible weaving constructed self-powered pressure sensor enabling continuous diagnosis of cardiovascular disease and measurement of cuffless blood pressure. *Adv. Funct. Mater.* **29**, 1806388 (2019).
55. J. Lin *et al*., Laser-induced porous graphene films from commercial polymers. *Nat. Commun.* **5**, 5714 (2014).
56. C. Poon, Y. Zhang, "Cuff-less and noninvasive measurements of arterial blood pressure by pulse transit time" in *2005 IEEE Engineering in Medicine and Biology 27th Annual Conference* (IEEE, 2006), pp. 5877–5880.